I&EC research
Industrial & Engineering Chemistry Research
pubs.acs.org/IECR
Article

Additively Manufactured Zirconia-Supported Indium Oxide Catalysts and Their Performance in Direct Methanol Synthesis

Emiliano S. Dal Molin,* Mudassar Javed, Georg Brösigke, Maik Alexander Rudolph, Jens-Uwe Repke, Reinhard Schomäcker, Ulla Simon, Maged F. Bekheet,* and Aleksander Gurlo

Cite This: *Ind. Eng. Chem. Res.* 2025, 64, 1032−1045

Read Online

ACCESS | Metrics & More | Article Recommendations | Supporting Information

ABSTRACT: In_2O_3/ZrO_2-based materials are emerging as candidates for the next generation of industrial catalysts for direct methanol synthesis. In this research, such catalysts were additively manufactured into two distinct geometries that exhibit different pressure drops and activity profiles, both among themselves and in comparison to extrudates. The monoliths produced were comprehensively characterized using a range of techniques, including gas sorption, X-ray diffraction, micro X-ray fluorescence, and Raman mapping, to verify their phase and chemical composition. Computational fluid dynamics was employed to simulate the gas flow through these structures, corroborating that the variations in the accessible surface area are the reason for changes in their performance. Furthermore, the postreaction characterization provides some insight into the catalysts' degradation mechanisms under hydrogen-rich conditions, identifying the migration of indium oxide to the catalyst surface and pore blocking as possible causes of the loss of activity.

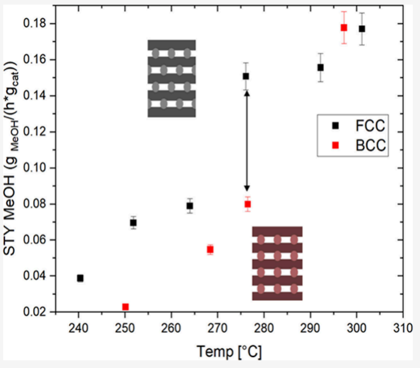

1. INTRODUCTION

A variety of strategies are being investigated to address the ongoing average global temperature increase caused by the greenhouse effect, which is predominantly attributed to the inordinate levels of carbon dioxide in the atmosphere. Among these, carbon capture and utilization (CCU) stands out as a particularly promising long-term solution. CCU encompasses an array of processes designed to extract CO_2, in its various forms, from the atmosphere and repurpose it either by converting it into fuels or by integrating it into novel materials.[1−3]

Direct methanol synthesis (R1) is identified as one of the key processes capable of facilitating carbon capture and recycling. Methanol (MeOH), derived from CO_2, is acknowledged for its versatility, holding potential as a renewable, net carbon-zero fuel and serving as a reagent in a number of industrial chemical processes.[4] Pioneering industrial initiatives, such as the carbon recycling international's (CRI) demonstration plant in Iceland, are progressively focusing on the utilization of direct methanol synthesis as their principal process.[5] This process faces several challenges, including the necessity of high pressures, which result in elevated operational expenses (OPEX) due to the requirement for substantial pumping equipment, particularly if there is a significant pressure drop across the reactor bed. Currently, MeOH production is mainly carried out with synthesis gas using copper−zinc−alumina-based catalysts at a pressure of 50 bar (and more) and temperatures of 250−300 °C. Additionally, precise thermal control is essential to mitigate the formation of CO through the competing reverse water gas shift reaction (RWGS, R2), which is favored at elevated temperatures. This control is also crucial to maximize the effectiveness of the catalyst used. Furthermore, there is a potential risk of MeOH decomposition to CO via R3, another process that is favored at higher temperatures and should be avoided.[1]

$$CO_2\,(g) + 3H_2\,(g) \rightleftharpoons CH_3OH\,(g) + H_2O\,(g) \qquad \Delta\bar{H}^\circ_{298\,K} = -49.5\ \mathrm{kJ/mol}_{CO_2} \tag{R1}$$

$$CO_2\,(g) + H_2\,(g) \rightleftharpoons CO\,(g) + H_2O\,(g) \qquad \Delta\bar{H}^\circ_{298\,K} = +41.2\ \mathrm{kJ/mol}_{CO_2} \tag{R2}$$

$$CH_3OH\,(g) \rightleftharpoons CO\,(g) + 2H_2\,(g) \qquad \Delta\bar{H}^\circ_{298\,K} = +90.6\ \mathrm{kJ/mol}_{CO} \tag{R3}$$

Recently, zirconium oxide has proven to be a suitable catalyst support for methanol production.[6−10] In particular, catalysts based in indium oxide supported on monoclinic zirconia have

Received: September 11, 2024
Revised: November 18, 2024
Accepted: December 12, 2024
Published: January 4, 2025

attracted considerable attention due to their enhanced MeOH selectivity, superior stability, and straightforward synthesis.[8,9,11−16] However, the augmented activity of these catalysts poses a potential risk of hotspots and reactor runaways, especially when operated at high conversion rates.

The integration of additive manufacturing (AM) into the production of catalysts offers a promising solution for processes that require low pressure drops, efficient heat control, and highly active catalysts.[17−19] Particular attention has been paid to robocasting or direct ink writing (DIW). Robocasting is a material extrusion technique in which the material is deposited from the paste layer by layer in direct succession.[20] Target materials are commonly mixed with a binder and then extruded with a programmatically controlled mobile extruder (also known as a print head). The printed part is usually dried and undergoes a calcination procedure afterward. The use of direct ink writing to produce geometries that are not possible with other methods was first explored in the 2000s.[21−23] Its application in chemical engineering, particularly in fabricating monolithic catalytic supports with nonuniform cross-sections, followed shortly.[24] This innovation has been associated with enhanced activities, reduced pressure drops, and increased flow speeds, contingent on the specific geometry of the structure.[25−27] However, significant activity in this field only surged in recent years, fueled by the widespread availability of 3D printers in laboratories and the maturation of these techniques to accommodate a diverse range of processing conditions.[28,29] Outstanding results have been shown in the application of AM catalytic supports in a variety of reactions like CO_2 methanation,[27,30] the Suzuki and Sonogashira cross-couplings and a copper alkyne−azide cycloaddition,[31−33] MeOH condensation to dimethyl ether[34] and to olefins (MTO),[35] CO_2 splitting,[36] oxidative coupling of methane (OCM),[37,38] among others.[19,23] These reports often include better stability and higher activities, sometimes attributed to the reduction of reactor inhomogeneities ("hot- or cold-spots"), better gas phase mixing behavior, and more efficient catalyst spatial distribution.

In this study, we demonstrate the application of these techniques to direct methanol synthesis. We fabricate two distinct woodpile structures using a mesoporous monoclinic ZrO_2 support combined with a commonly used industrial binder. We investigate how these geometries influence the catalyst's performance under industrially relevant conditions (45 bar and up to 300 °C) and demonstrate that variations in printed catalyst geometry can lead to markedly distinct activity profiles. Our approach prioritizes a straightforward preparation method that is suitable for upscaling. The activity of additively manufactured samples is compared to that of extrudates and powder, contrasting with traditionally manufacturable catalyst geometries. Hydrogen-rich conditions and high flow speeds are used to maximize the yield.

Catalyst geometries, namely BCC and FCC (body-centered cubic and face-centered cubic, respectively), were selected from previous works[30,39−41] because they provide two well-differentiated gas paths, and their structures are otherwise not easily achievable by subtractive manufacturing or extrusion. These designations correspond to the lattice symmetry of these woodpile structures[42,43] and are sometimes also referred to as "1−1" and "1−3",[39] although no unified nomenclature exists. The BCC geometry with line-of-sight channels can allow for mostly undisturbed gas flow, while the FCC geometry with "zig-zag" channels can force the gas path to split and recombine after every layer. In spite of their differences, the structures have translational symmetry (in stark contrast to the randomly packed extrudates and powders) and can be represented by simple "unit cells" which greatly simplifies their simulation.

Moreover, we employ computational fluid dynamics (CFD) to simulate and understand the gas flow behavior, correlating these simulations with the experimental results under varying flow speeds and temperatures, showing that under the testing conditions there is a negligible contribution of turbulence and corroborating the idea that the driver behind the increase in activity is the increased accessible surface area. Kinetic data show limiting regimes and under which ranges they appear. To ensure the consistency of our findings, we comprehensively characterize the catalyst surfaces through X-ray-based methodologies, scanning electron microscopy (SEM), and Raman mapping to exclude differences in composition, distribution, and structure. We further utilized these tools to characterize the catalysts after catalytic tests to evaluate the impact of exposure to reaction conditions on their structural properties.

2. MATERIALS AND METHODS

2.1. Chemicals. Monoclinic zirconia pellets (ZrO_2, 1/8 in. pellets, prod. nr. 43814, SSA = 51 $m^2\ g^{-1}$), bentonite, sodium form ($Al_2H_2Na_2O_{13}Si_4$, prod. nr. A15795, NaBent), and indium nitrate hydrate ($In(NO_3)_3 \cdot x\ H_2O$, 99.99% (metal basis), prod. nr. 40185) were obtained from Alfa Aesar (Thermo Fisher Scientific, Germany). Methocel F50 (hydroxypropylmethylcelullose, MF50) was purchased from Dow Chemical Company (U.S.A.). All experiments were carried out with deionized water (DIW). CO_2, H_2, and N_2 (purity, 3.0 technical) were purchased from Linde Gas (Linde GmbH, Germany). Indium oxide (In_2O_3, 99.99% trace metal basis, prod. nr. 289418) was obtained from Sigma-Aldrich (Merck Ka, Germany). $In(OH)_3$ was synthesized hydrothermally using a procedure reported elsewhere.[44]

2.2. Additive Manufacturing of Zirconia Monolithic Supports. Zirconia pellets were milled with a vibrating disk mill (Type TS.250, Siebtechnik GmbH, Germany) for 3 min and sieved through a 100 μm sieve. The passing fraction was then rinsed in deionized water (DIW) and dried at 50 °C in a drying cabinet (T 6060, Heraeus, Germany), and used to prepare the rest of the samples. The powder was analyzed by XRD (see Section 2.4 for details) and was found to be monoclinic zirconia, with no other phases present.

NaBent (2g or 8 wt %) as the inorganic binder, milled zirconia (10 g or 40.2 wt %), and MF50 (0.9 g or 3.6 wt %) as an organic binder were well mixed using a rotary mixer (RW16 basic, IKA-Werke GmbH & Co. KG, Germany) until a homogeneous mixture was achieved. Afterward, DIW (12 g or 48.2 wt %) was slowly added until a printable slurry was formed.

The slurry was then loaded into a transparent polypropylene (PP) syringe barrel (30 mL, Vieweg, Germany) with a Luer lock to which a 0.84 mm straight metallic dispensing tip (Vieweg, Germany) was connected. This barrel was then loaded onto an Ultimaker 2+ connect 3D printer (Ultimaker, Netherlands) with a modified print head that accommodates a PP syringe, as described in a previous work involving mesoporous silica.[45] Slurry extrusion was achieved by employing pressurized air at 4−6 bar, while the printing speed was 7 mm s^{-1} and the layer height was 0.5 mm. Printing was carried out at room temperature. The monoliths were fabricated in a layer-by-layer fashion in two differing structures comprised of layers of alternating directions, BCC and FCC (Figure 1c and Figure 1g). Geometries were designed following previous works by our group,[45,46] and layer height was selected to be as small as possible while maintaining printability, with the limits being dictated by the maximum system pressure and stepper motor Z axis resolution. $X-Y$ fiber spacing was chosen to be one nozzle diameter, although this is not conserved due to eventual shrinkage. In the case of BCC structures, these layers are aligned with respect to each other, while the FCC structures feature an offset of half of the channel size. Both structures have the same geometrical porosity (ca. 60%, considering the 0.84 mm fiber diameter). All monolith designs had a square cross-section of 20 × 20 mm^2 and 8 mm in height. The structures were designed in FreeCAD (Juergen Riegel, Werner Mayer, and Yorik van Havre (2001−2017)). FreeCAD (version 0.19 [Software] available from http://www.freecadweb.org), and the corresponding G-CODE for their printing was generated through a custom-made Python script.

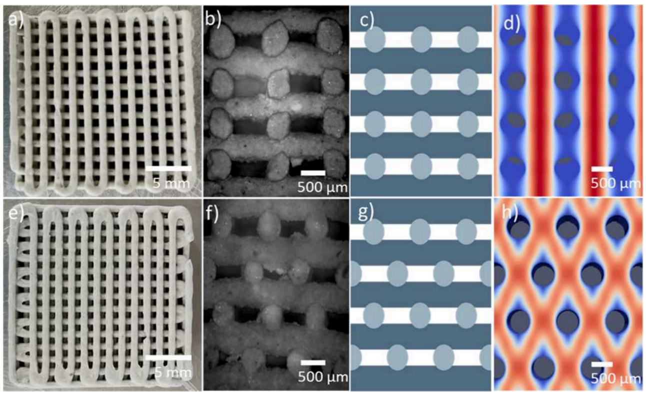

Figure 1. (a) BCC structure, as printed, top view. (b) Optical microscope image of a calcined BCC structure (cross-sectional view). (c) Schematic cross-section of a BCC structure. (d) CFD simulation results for a BCC structure (red, high gas velocity magnitude; blue, low gas velocity magnitude; flow direction, bottom-to-top; $R_e = 0.5$; $U_0 = 3.6 \times 10^{-3}$ m·s^{-1}; WHSV = 50,000 mLs_{Feed} h^{-1} $g_{cat}{}^{-1}$). (e) FCC structure, as printed, top view. (f) Optical microscope image of a calcined FCC structure (cross-sectional view). (g) Schematic cross-section of an FCC structure. (h) CFD simulation results for an FCC structure (red, high gas velocity magnitude; blue, low gas velocity magnitude; same color scale and conditions as (c)).

The obtained structures were dried for 24−48 h in a partially opened moisture-saturated desiccator to ensure a slow drying procedure and to avoid the formation of cracks. Once dried, the structures were calcined in a laboratory oven (K 114, Heraeus, Germany), from room temperature (RT) to 300 °C in 10 h (0.5 °C min^{-1}) and 300 to 600 °C in 5 h (1 °C min^{-1}) with dwelling at 600 °C for 2 h and then allowed to reach room temperature by passive cooling. Extrudates were produced in a similar way by extruding the slurry through a 2.6 mm nozzle and cutting it every 5 mm.

2.3. Catalyst Loading. After calcination, the monoliths were cut into cylindrical structures of about 6 mm diameter and 6 mm height using an M3400 diamond wire saw (Well Diamantdrahtsägen GmbH, Germany). The monoliths were submerged in a solution containing 0.67 g/mL of $In(NO_3)_3 \cdot xH_2O$ that was dried overnight in a vacuum furnace (Heraeus VT 5042 EK, Heraeus, Germany) at 65 °C. The submerged monoliths, still in the solution, were then put in a vacuum furnace at room temperature with a vacuum applied overnight to ensure complete filling of the pores. Extrudates were handled similarly.

Afterward, the monoliths and extrudates were removed from the solution and subsequently dried with compressed air to aid with the removal of any excess solution from the open spaces in the structure. The monoliths were then dried at 65 °C for 12 h and calcined at 450 °C for 3 h under air, utilizing a heating rate of 5 °C min^{-1}, after which they were passively cooled down. Samples after this treatment are named InZrOx-# (where # = BCC for the BCC structures, FCC for the FCC structures, E for the extrudates, or P for the powdered catalyst). Additionally, the suffixes -F (for fresh catalyst) and -S (for spent catalyst) are added where relevant. Reference extrudates were functionalized in the same way and are referred to as "In_2O_3/ZrO_2 Ref." where relevant.

The powdered catalyst was obtained by hand grinding the extrudates with a mortar after In_2O_3 loading, followed by sieving through a 100 μm sieve. Reference extrudates were used as received from the manufacturer. Synthetic samples Na-Bent-10 and Na-Bent-20 were prepared by weighing the necessary amounts of c-In_2O_3, m-ZrO_2, and Na-Bent (weight fractions, 1:8:1 and 1:7:2, respectively; total mass, 1 g) and mixing and milling the resulting powder in an agate mortar until a homogeneous mixture was formed.

2.4. Structural Characterization. High-resolution synchrotron X-ray diffraction (HR-XRD) characterization was carried out for InZrOx-P-F and -S at beamline 12.2.2 of the Advanced Light Source facility at the Lawrence Berkeley National Laboratory, California. Diffraction patterns were collected in angle-dispersive transmission mode with a focused 25 keV monochromatic beam (λ = 0.4952 Å). Laboratory powder X-ray diffraction (XRD) measurements were performed using a D8 ADVANCE X-ray diffractometer (Bruker AXS GmbH, Germany) equipped with a Lynx Eye 1D detector with a copper radiation source (λ (Kα) = 1.542 Å). The measurements were carried out in a Bragg−Brentano geometry and a divergence slit of 0.5°. The 2θ angles from 10° to 80° were collected in 0.020° increments with 3 s per increment at RT. Samples were ground with an agate mortar before the X-ray diffraction experiments were conducted. Rietveld refinement (RR) was performed using the FULLPROF program[47] and profile function 7 (Thompson−Cox−Hastings pseudo-Voigt convoluted with an axial divergence asymmetry function).[48] The resolution function of the instrument was obtained from the structure refinement of a LaB_6 NIST 660b standard.

Determination of the indium content in the catalysts (InZrOx-E-F, InZrOX-BCC-S, and InZrOX-FCC-S) was performed with inductively coupled plasma optical emission spectroscopy (ICP-OEM) in a Horiba Scientific ICP Ultima2 instrument (Horiba, Kyoto, Japan). Samples were cut in half with a diamond wire saw and crushed. The crushed samples were then digested in an aqueous suspension with the addition of HNO_3 and HF at 200 °C for 5 h in an autoclave.

In order to determine the distribution of indium in whole monoliths, elemental mapping was performed on various cross-sectional samples using a Bruker M4 Tornado μ-XRF equipped with an X-ray focusing capillary optic and two 30 mm^2 silicon drift detectors. Mappings were performed by using a 20 μm spot size. The Rh-anode was operated at a 50 kV acceleration voltage and an anode current of 600 mA at a chamber vacuum of 20 mbar. Spots were set at intervals of 20 μm and measured for 90 ms, yielding a total mapping time of about 24 h per polished block. The energy position of the fluorescence lines and the power of the X-ray tube are calibrated monthly using a set of single-element standards provided by Bruker (Germany). New fresh samples (InZrOx-BCC-F and InZrOx-FCC-F) were synthesized for this measurement, as the need to cut them to provide a cross-section naturally destroys the sample.

The specific surface area of printed, calcined, and cut monoliths was studied by nitrogen sorption analysis in a QuadraSorb Station 4 apparatus (Quantachrome, USA). Isotherms were recorded at 77 K after degassing the specimens for 12 h at 200 °C under a vacuum. The surface area was determined using the Brunauer, Emmet, and Teller (BET) method using data in the 0.05−0.35 P/P_0 range. Pore volume was calculated through the Barrett−Joyner−Halenda (BJH) method. All nitrogen sorption data were analyzed using QuadraWin (ver. 5.05, Anton Paar QuantaTec Inc.) software. Gas sorption was performed on InZrOx-BCC-F and -S and InZrOx-FCC-F and -S and on nonfunctionalized samples and raw materials.

Scanning electron microscopy (SEM) was carried out at the Center for Electron Microscopy (ZELMI) of the TU Berlin with a ZEISS GEMINI SEM500 NanoVP microscope (Carl Zeiss AG, Germany), coupled with a Quantax XFlash 6|60 EDX system (Bruker Corporation, USA) to confirm μ-XRF results at a higher spatial resolution. Obtained maps were further analyzed through the use of the ESPRIT software suite (Bruker Corporation, USA). SEM was performed on InZrOx-BCC-F and -S and InZrOx-FCC-F and -S.

Raman scattering at room temperature was induced by a 532.16 nm frequency-stabilized single longitudinal mode diode-pumped solid-state (DPSS) laser (Laser Quantum Torus 532) on a LabRAM HR 800 spectrometer (Horiba Jobin-Yvon). The laser beam was focused onto the sample using a 100x (for reference samples) or a 10x (for mapping) Olympus objective with the scattered light being collected in backscattering geometry. Backreflected and elastically scattered light (Rayleigh component) was filtered using an ultralow frequency filter (ULF) unit and then spectrally dispersed by a monochromator with a grating of 1800 lines/mm. The light was detected by a charge-coupled device (CCD). The spectral dispersion of the setup is 0.35 cm^{-1}/pixel. Using the 1800 lines·mm^{-1} grating, the spectral resolution at 550 nm (610 cm^{-1}) is about 0.7 cm^{-1}. Reference samples were measured for 12 min. Mapping was achieved by robotically moving the sample stage in 20 μm increments and scanning the sample for 2 min. The typical total time for a full map was 16 h. Data were processed with a Whittaker−Eilers smoother[49] and EMSC (extended multiplicative signal correction).[50] Signal maps were generated with QUASAR (v.1.9.0, obtainable from https://quasar.codes/download/).[51,52]

The XAFS measurements were performed at the P64 beamline, DESY.[53] A Si(111) monochromator was used for scanning the energy. The sample was loaded in an in situ cell prepared to sustain high temperatures and pressures, described elsewhere.[54] The XAFS measurements were performed in fluorescence and transmission modes simultaneously. The transmission and fluorescence signals were recorded using an ionization chamber and a passivated implanted planar silicon (PIPS) detector. The data displayed in this work were obtained in the fluorescence mode. Before normalization, measurement artifacts were removed manually. Edge position was determined as the energy at which the first derivative of the spectrum had a maximum. Temperature was set at 295 °C, pressure was set at 4.5 MPa, and gas compositions (Ar, H_2, and CO_2) were pure Ar and 1:8:1 Ar:H_2:CO_2. Total flow = 25 mL·min^{-1}, catalyst weight ca. 10 mg. Reference samples were measured under ambient conditions.

2.5. Catalytic Testing.

The testing setup for the catalytic performance of all catalysts consisted of three mass flow controllers (MFC), a plug flow reactor (8 mm in diameter, 40 cm in length), and an online gas chromatograph (Agilent μGC 490) equipped with CPMolsieve 5 Å and PoraPLOT Q columns able to measure CO_2, H_2, N_2 CO, MeOH, and H_2O. To avoid gas bypass, the monoliths were positioned roughly in the middle of the reactor, supported in place by the thermocouple, into a stainless-steel ring with a diameter of 8 mm and wall thickness of ca. 1 mm in order to ensure maximum contact between the printed structures and the reactor walls. The downstream lines were heated and insulated to avoid product condensation. This setup is schematized in Figure S1.

Quantities and catalytic parameters were calculated using the following equations:

$$\mathrm{WHSV}\left(\frac{\mathrm{mLs_{Feed}}}{\mathrm{h*g_{cat}}}\right) = \frac{F}{w_{\mathrm{cat}}} \tag{1}$$

$$X_{\mathrm{CO_2}}\ (\%) = \frac{x_{\mathrm{CO_2,in}}*\overline{F}_{\mathrm{in}} - x_{\mathrm{CO_2,out}}*\overline{F}_{\mathrm{out}}}{x_{\mathrm{CO_2,in}}*\overline{F}_{\mathrm{in}}}*100 \tag{2}$$

$$S_j\ (\%) = \frac{x_{\mathrm{j,out}}}{\sum_{\mathrm{j}} x_{\mathrm{j,out}}}*100,\ j = \mathrm{MeOH,\ CO} \tag{3}$$

$$\mathrm{STY_{MeOH}}\left(\frac{\mathrm{g_{MeOH}}}{\mathrm{h*g_{cat}}}\right) = \frac{x_{\mathrm{CO_2,in}}*\overline{F}_{\mathrm{in}}*X_{\mathrm{CO_2}}*S_{\mathrm{MeOH}}*M_{\mathrm{MeOH}}}{w_{\mathrm{cat}}}/10000 \tag{4}$$

$$r_{\mathrm{j}}\left(\frac{\mathrm{mol_j}}{\mathrm{h*g_{cat}}}\right) = \frac{x_{\mathrm{j,out}}*\overline{F}_{\mathrm{out}} - x_{\mathrm{j,in}}*\overline{F}_{\mathrm{in}}}{w_{\mathrm{cat}}},\ j = \mathrm{MeOH,\ CO,\ CO_2} \tag{5}$$

where j stands for MeOH, CO, or CO_2. mLs is "standard milliliters", that is, milliliters of gas as measured at 20 °C and 1013.25 hPa(a), h is hours, g_{cat} is grams of catalyst loaded in the reactor, and g_{MeOH} is grams of MeOH produced. X_j is the conversion percentage of the component j, x_j is the molar fraction of the component j at the inlet or outlet, $\overline{F}$ is the total hourly molar flow at the inlet or outlet (obtained from feed composition and volumetric flow or from reconciliation algorithm, see Supporting Information), S_j is the selectivity toward product j, M_j is the molar mass of component j, STY_j is the space-time yield of product j, r_j is the rate of generation of component j, and w_{cat} is the weight of the catalyst introduced. Equation 4 has a factor of 10,000 to turn the selectivity and conversion (reported in %) to fractions.

Standard conditions for all tests: W8 hly space velocity (WHSV)= 50,000 mLs_{Feed} h^{-1} $g^{-1}{}_{cat}$; temperature = 568 K; CO_2:H_2:N_2 = 1:8:1; pressure, 4.5 MPa; and catalyst weight, ca. 275 mg.

Reaction rate data obtained during the temperature variation experiments was fitted according to the modified Arrhenius equation:

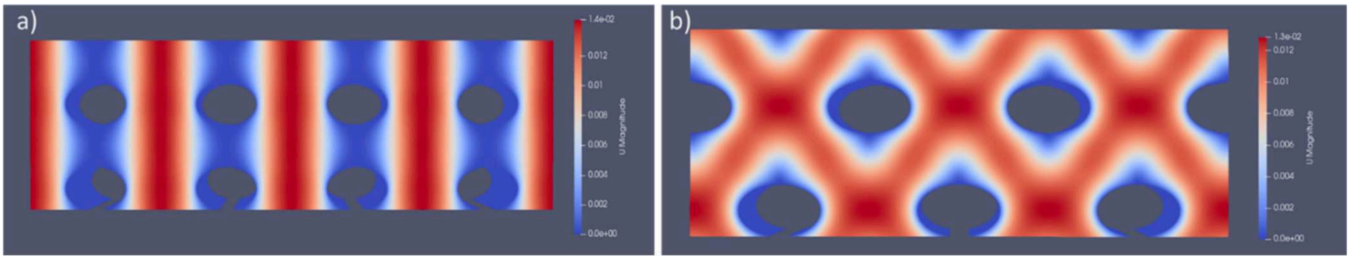

Figure 2. Simulated flow velocity profile and isovelocity surfaces across BCC and FCC geometries; $R_e = 0.5$; $U_0 = 3.6 \times 10^{-3}$ m·s^{-1}; WHSV = 50,000 mLs$_{\text{Feed}}$ h^{-1} g$_{\text{cat}}$$^{-1}$. (a) Reconstruction of an extended BCC system through translations and reflections of the BCC unit cell. (b) Reconstruction of an extended FCC system through translations and reflections of the FCC unit cell.

$$\ln(r) = \ln(A') - \frac{E_a}{R}\left(\frac{1}{T}\right) \tag{6}$$

where r is the rate of reaction per unit weight of the catalyst and A' is the Arrhenius pre-exponential factor multiplied by the corresponding product and reactant concentrations according to the model (modified Arrhenius preexponential factor). This equation is only valid for a system working under the kinetic regime (see the SI for clarification).

2.6. CFD Simulation. The flow was described using CFD to analyze, evaluate, and compare the flow patterns in the different structures (FCC vs BCC). The open-source library OpenFOAM (version 9, The OpenFOAM Foundation, Ltd.) was used for meshing (blockMesh + snappyHexMesh) and simulation (simpleFoam) of a laminar, steady state, incompressible flow ($\nu = 6 \times 10^{-6}$ m^2 s^{-1} (air @25 °C)) at the same Reynolds number as the catalyst characterization was carried out. The domain for the simulation was reduced to the smallest repeating pattern ("unit cells" FCC 0.75 × 0.75 × 1.5 mm^3, 1,367,760 cells; BCC 0.75 × 0.75 × 0.75 mm^3, 649,153 cells) of each structure, as depicted in Figure S5a, so that periodic boundary conditions were applied for inlet/outlet and symmetric boundary conditions elsewhere at the domain where no walls were located. The periodic boundary conditions are implemented such that the mean velocity (representing the volume flow or mass flow in an incompressible fluid, respectively) is kept constant by adjusting a source term for pressure force to compensate the pressure loss. Holes in the mesh correspond to the printed monolith fibers and are elliptical, with the long axis measuring 0.6 mm and the short one 0.375 mm to account for shrinkage after calcination.

2.7. Equilibrium Simulations. Equilibrium simulations were carried out using the CANTERA Python library.[55] Thermodynamical data was obtained from NASA's Thermobuild tool (https://cearun.grc.nasa.gov/ThermoBuild/), and a system comprising of one mole (in total) of N_2, H_2, CO_2, CO, MeOH, and H_2O (initial composition 1:8:1:0:0:0, respectively) pressurized at 4.5 MPa and varying temperatures in the range 200−300 °C in 1 °C increments was considered. The isothermal thermodynamic equilibrium concentrations were then calculated. Detailed code and input thermodynamic data files can be found in the Supporting Information. Weight-normalized equilibrium rates were calculated by calculating the converted fraction of moles of CO_2 at equilibrium and multiplying it by the hourly molar flow at 50,000 mLs$_{\text{Feed}}$ h^{-1} g$_{\text{cat}}$$^{-1}$ WHSV, as follows:

$$r_{CO_2,\max}\left(\frac{\text{mol}_{CO_2}}{\text{h}*\text{g}_{\text{cat}}}\right) = \frac{\left(x_{CO_2,\text{eq}}\frac{\overline{F}_{\text{out,eq}}}{\overline{F}_{\text{in}}} - x_{CO_2,\text{in}}\right)*\text{WHSV}}{24{,}055\ \frac{\text{mLs}}{\text{mol}}} \tag{7}$$

$$r_{j,\max}\left(\frac{\text{mol}_j}{\text{h}*\text{g}_{\text{cat}}}\right) = r_{CO_2,\text{eq}}*S_{j,\text{eq}}/100 \tag{8}$$

3. RESULTS AND DISCUSSION

3.1. Geometry and Flow Simulation of Printed Monoliths. Figure 1b and Figure 1f display the optical images of the investigated printed monoclinic ZrO_2 (m-ZrO_2) supports with BCC and FCC structures, respectively, after drying and calcination, prior to the functionalization with cubic In_2O_3 (c-In_2O_3). These structures have a key structural difference: where the BCC monolith has straight channels, the FCC structure has bifurcating paths at every other layer due to the changing position of the struts (Figure 1c and Figure 1g). This significant difference in the structure directly impacts the flow behavior of the gas, which is pictured in Figure 1d and Figure 1h. The FCC structure has a much better flow distribution, eliminating the zones of very low flow velocity magnitude ("dead spots") present between the struts of the BCC structure.

After calcination, the structures shrank due to water loss and subsequent sintering, resulting in a linear shrinkage of 25%. The magnitude of this shrinkage is consistent with similar formulations in our previous work.[45] The cross-sections of the printed and sintered supports can be seen in the optical microscopy images shown in Figure 1b and Figure 1f. For testing in the reactor, the approximately 6 mm cylinders were cut from the samples so that they would fit into the reactor (see Figure S2). The cut-outs are not perfectly cylindrical due to the brittleness of the thin ceramic struts near the edges and the mechanical stresses created by the diamond saw. This deviation may slightly affect the catalytic results as a small amount of the flow around the structure passes through a section with a smaller amount of catalyst.

The obtained CFD results are summarized in Figure 2, where the calculated velocity fields for both structures is shown. The calculated Reynolds number for the flow entering the monolith channels is 0.5 (for a WHSV of 50,000 mL$_{\text{sFeed}}$ h^{-1} g$_{\text{cat}}$$^{-1}$), far from the turbulent regime. As a natural consequence of mass conservation, the flow accelerates from its initial input velocity when it enters the volume occupied by the catalysts. The differences in the generated velocity profiles are readily apparent (additional data in Figure S5). The BCC structure (Figure 2a) shows a slightly higher maximum velocity magnitude ($U_{\max,\mathrm{BCC}} = 0.014$ m·s^{-1} vs $U_{\max,\mathrm{FCC}} = 0.013$ m·s^{-1}) in the center of the "channels" but significantly lower close to the walls (almost 0 directly behind the struts, except for a small portion of the wall which is directly perpendicularly oriented to the direction of flow). In contrast, the results for the FCC structure (Figure 2b) show a more uniform velocity distribution. Additionally, due to the offset between the layers, the FCC structure generates a reorientation (or rather a split) of the bulk flow every two layers. This has a double impact: on one hand, it creates a more uniform velocity distribution close to the catalyst surface (the "bends" in the mesh). On the other hand, as can be appreciated in Figure 2b and Figures S5d and S5e, the flow of the FCC structure adapts much better to the support and follows its contour, reducing the "dead spots" where flow is stagnant. These results present some resemblance to the "analogous" 2D case of a flow going through a stack of tubes, in an inline (BCC) or a staggered (FCC) configuration.[56] Additionally, on the FCC cell, the velocity surfaces are much closer together (signifying a higher gradient in the normal direction and thus a thinner viscous boundary layer), as the flow tends to hit them head-on rather than grazing them (as is the case in the BCC cell) (see Figure S5e). The FCC geometry was also proven to generate better-mixed gas flows, as can be appreciated by the higher vorticity developed by the flows when compared to the BCC structure (Figure S5d and S5e).[57] This higher utilization of the surface has clear consequences for the catalytic activity, as can be appreciated in the next section.

Finally, pressure drop (Figure S6 and Figure S7) was calculated for the two structures, resulting in drops of 3.3 and 2.2 Pa·m^{-1} for the FCC and BCC structures, respectively, in agreement with the trends found in other simulations.[41] To make a comparison, if a set of extrudates is taken with dimensions similar to the dimension of struts of these monoliths (0.5 mm in diameter and 1 mm in length) and randomly packed in a similar reactor, the predicted pressure drop (by the Ergün equation) is about 27.6 Pa·m^{-1} at the velocities used in this work. (see SI Section 2 for calculation details.) The comparison of the pressure drop of FCC/BCC structures to straight channeled monoliths has been the subject of previous works, finding a similar trend ($\Delta P_{\mathrm{FCC}} > \Delta P_{\mathrm{BCC}} > \Delta P_{\mathrm{honeycomb}}$).[25]

3.2. Catalytic Performance.

In order to measure the catalytic performance of the samples, several plug flow reactor experiments were carried out, and outgoing concentrations of N_2, H_2, MeOH, CO, and CO_2 were measured. Equilibrium concentration simulations as a function of temperature in the studied range are provided as a guide in Figure S3, where it can be seen that increasing the starting H_2 concentration increases the selectivity toward MeOH, especially at higher temperatures. The equilibrium yield of MeOH was also simulated and mapped, and projections at the studied temperature and pressure were taken, which show the significant effect of temperature on the system and are shown in Figure S4. In short, the direct MeOH synthesis from CO_2 is a doubly limited reaction: MeOH is not the favored product at high temperatures (thermodynamic limitation), and catalyst activity drops at lower temperatures (kinetic limitation). The simulation also illustrates the system's sensitivity toward temperature, as even a 10 °C change has a noticeable impact on the equilibrium yield of MeOH. In addition, the activity of different raw material combinations was evaluated to investigate a potential interaction of the added binder. The results of these catalytic tests (Figure 3) reveal the negligible effect of the sodium bentonite binder and the ZrO_2 support, as well as c-In_2O_3 that has been adsorbed on the binder. In line with the CFD results, we can notice a higher activity of the FCC catalyst compared to its BCC counterpart. In addition, it shows similar product distribution for InZrOx-P, -E, and -BCC and the In_2O_3/ZrO_2 reference but a markedly different one for InZrOx-FCC. InZrOx-P shows a reduced activity, which could be the result of gas flow channeling through the powder bed and is therefore not explored further.

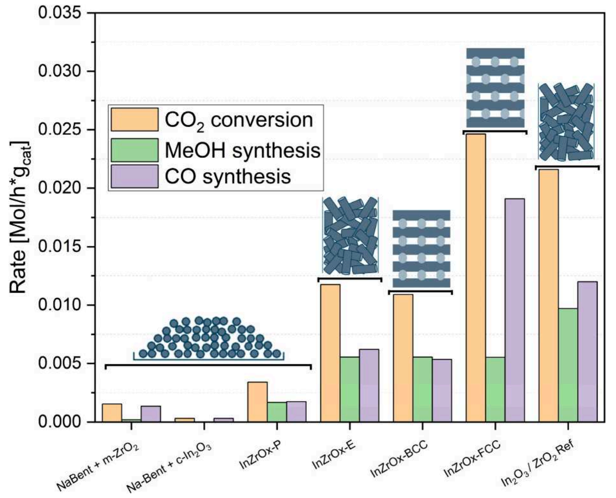

Figure 3. Rate data for different component mixtures and tested samples (InZrOx-P, -E, -BCC, and -FCC) as well as the In_2O_3/ZrO_2 internal reference. Standard conditions for all tests: weight hourly space velocity (WHSV) = 50,000 mLs$_{\mathrm{Feed}}$ h^{-1} g$_{\mathrm{cat}}$$^{-1}$; temperature = 568 K; CO_2:H_2:N_2 = 1:8:1; pressure = 4.5 MPa; catalyst weight, ca. 275 mg.

Figure 4a shows the CO_2 hourly molar consumption rate in the WHSV range of 20,000−50,000 mLs$_{\mathrm{Feed}}$ h^{-1} g$_{\mathrm{cat}}$$^{-1}$, where a significant difference in activity can be seen between two monolithic structures (0.025 mol h^{-1} g$_{\mathrm{cat}}$$^{-1}$ for the InZrOx-FCC vs 0.009 mol h^{-1} g$_{\mathrm{cat}}$$^{-1}$ for InZrOx-BCC, at their maximum). Higher activity of FCC-type structures when compared to BCC ones have been seen in other work in the literature for other systems[30,35,39] and attributed to higher mixing due to turbulence and higher contact area and residence times, although no detailed kinetic analyses were performed. InZrOx-BCC exhibits a lower CO_2 consumption rate, reaching seemingly a plateau at 40,000 mLs$_{\mathrm{Feed}}$ h^{-1} g$_{\mathrm{cat}}$$^{-1}$ WHSV, whereas the InZrOx-FCC's CO_2 consumption grows with higher gas velocities and a clear plateau is not reached. The absence of a plateau hints toward the catalyst still operating outside of the kinetic regime. In contrast, the extrudates catalyst, InZrOx-E, possesses a markedly lower activity than the In_2O_3/ZrO_2 ref. Nevertheless, their trend matches to a reasonable extent, and the lower activity could be a consequence of the lower amount of active sites on the InZrOX-E sample, the binder lowering accessibility to active sites, or both. It is worth mentioning that InZrOx-FCC surpasses the CO_2 conversion rate per gram of the reference, despite suffering the same drawbacks as InZrOX-E. Figure 4b shows the selectivity toward MeOH in the same WHSV range. InZrOx-BCC displays a higher selectivity toward MeOH, while InZrOx-FCC has a noticeably lower one (51% vs 22% for InZrOx-BCC and InZrOx-FCC, respectively), even at similar

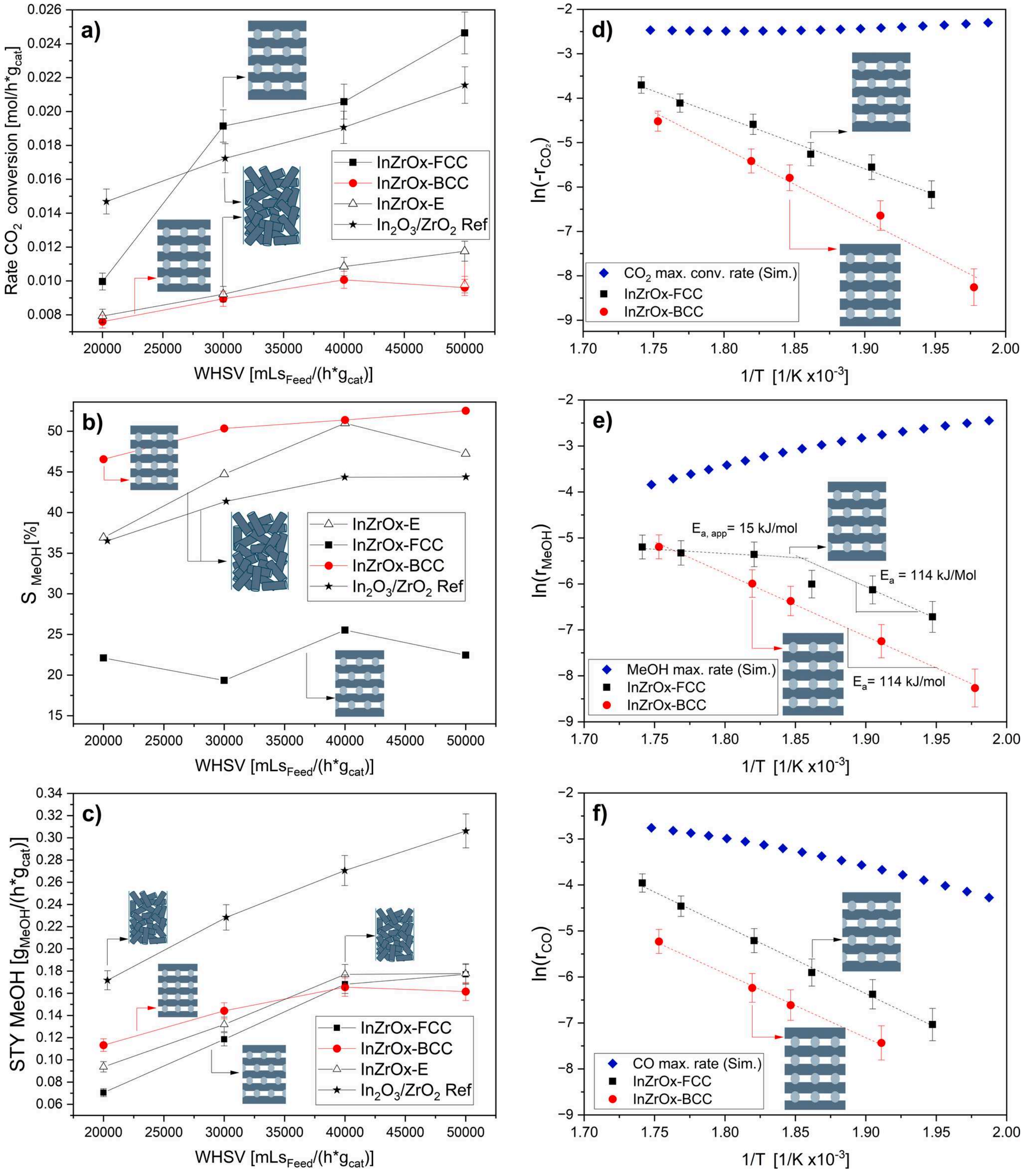

Figure 4. Summary of the performance of InZrOx-E, InZrOx-BCC, InZrOx-FCC, and the In_2O_3/ZrO_2 reference in catalytic tests. Standard conditions for all tests: Weight hourly space velocity (WHSV) = 50,000 mLs_{Feed} h^{-1} $g_{cat}{}^{-1}$; temperature = 568 K; CO_2:H_2:N_2= 1:8:1; pressure = 4.5 MPa; catalyst weight. ca. 275 mg. CO_2 conversion rate (a), selectivity toward MeOH (b), space-time yield of MeOH as a function of WHSV (c), and Arrhenius plots for CO_2 conversion (d), MeOH (e), and CO synthesis plus simulated maximum reaction rates (f) (corresponding to the reaction mixture at the outlet being at thermodynamic equilibrium). Only two experimental points were used in (e) to illustrate the slope at the low-temperature region for InZrOx-FCC as the data point at 265 °C (538 K) lies in a transition region between the two different regimes (mass-transfer and kinetically limited). The fifth data point in (f) was excluded due to a low concentration of CO that was below the detection limit of the used GC. All rates are normalized by catalyst mass.

CO_2 consumption rates (i.e., at 20,000 mLs_{Feed} h^{-1} $g_{cat}{}^{-1}$ WHSV). Once again, the effect of the geometry on product distributions has been reported,[39] and it was posited that it is the heat and mass transport properties that play a crucial role on the product distribution. Additionally, none of the structures show significant selectivity changes with WHSV. Notably, InZrOx-E and the In_2O_3/ZrO_2 reference show similar trends, which point toward a negligible contribution of the binder to selectivity. As a consequence of the variation on the CO_2 conversion rate, the space-time yield (STY) of MeOH for both monolithic structures show great variations across the range (reaching maxima of ca. 0.17 $g_{MeOH}\ h^{-1}\ g_{cat}{}^{-1}$ at 50,000 $mLs_{Feed}\ h^{-1}\ g_{cat}{}^{-1}$ WHSV for both structures), seen in Figure 4c, although they are much more pronounced in the case of InZrOx-FCC. The linearity of the increase of the MeOH STY seems to point toward a mass transfer limited regime once again, implying potentially higher activity at WHSVs higher than those explored in these experiments. Once again, InZrOx-BCC seems to hit a plateau at 40,000 $mLs_{Feed}\ h^{-1}\ g_{cat}{}^{-1}$ WHSV, consistent with the observed behavior in Figure 4a. In terms of MeOH production, In_2O_3/ZrO_2 is markedly superior to its additively manufactured counterparts, due to the lower activity of InZrOx-BCC and InZrOx-E and to the lower selectivity of InZrOx-FCC. While the absolute yield of MeOH for this reference may be somewhat lower than previous reported values,[11,58] it is important to remark that the lower surface area of the support (51 $m^2\ g^{-1}$ in this work vs 91 $m^2\ g^{-1}$in ref 11 and 120 $m^2\ g^{-1}$ in ref 58) could limit the activity.

To complement the WHSV variation studies and try to elucidate the origin of the selectivity change between the monolithic structures, Arrhenius plots were constructed for the consumption of CO_2 and the production of MeOH and CO (Figure 4d, Figure 4e, and Figure 4f, respectively). Figure 4d shows the difference between the rates of CO_2 consumption in the two geometries. Additionally, the maximum thermodynamic CO_2 consumption rate was simulated with the highest rate achieved by InZrOx-FCC being around 30% of the thermodynamic equilibrium values. The InZrOx-BCC catalyst shows a higher apparent activation energy for CO_2 consumption, indicated by its faster-growing rate with temperature. This is due to the lower rate of MeOH synthesis and lower apparent activation energy of the direct MeOH synthesis on InZrOx-FCC, whose Arrhenius plot can be seen in Figure 4e. The significant difference in behavior might be explained by mass transfer limitations appearing in the MeOH synthesis reaction in InZrOx-FCC. The mass transfer limitations become apparent when calculating the apparent activation energy of the MeOH formation. Due to the nonlinearity of the MeOH rate curve, no single "activation energy" can be obtained. If the activation energy is estimated with the two data points at lower temperatures (because the third point lies in a transition region), the result is in close agreement with InZrOx-BCC (ca. 114 kJ mol^{-1}). The activation energy calculated from InZrOx-BCC is around 10% off from reports in the literature.[8] At higher temperatures in InZrOx-FCC, the reaction becomes mass transfer limited, and the calculated apparent activation energy decreases to 15 kJ/mol, a value typical of mass transfer limited reactions as the gas flow can no longer supply a sufficient quantity of hydrogen to the surface of the structured catalyst. This variation illustrates the transition between the two regimes (Table 1).

The same does not happen for the RWGS reaction, which remains at the kinetic limit of the catalyst (Figure 4f), as it requires a lower amount of hydrogen.[8] Interestingly, this allows comparing the availability of the catalytic sites per unit gram of the catalysts (assuming that the sites for MeOH and RWGS are shared;[8] in addition, the surface areas are similar, $S_{BET,\ FCC}$= 35 $m^2\ g^{-1}$ and $S_{BET,\ FCC}$= 37 $m^2\ g^{-1}$, which rules out this difference being solely due to a higher specific surface area) from the intercept (i.e., $\ln(A')$, see the SI for details) of the best fitting curves (21.5 for the FCC catalyst vs 19.2 for the BCC one) for each catalyst geometry, which falls in line with the higher utilization of the surface by the flow going through the FCC structure, as shown in the previous section (see Figure 2). These results also explain the reduced selectivity in InZrOx-FCC and the need for a higher WHSV to reach the kinetic limit. The similarity of both activation energies suggests that the surface is chemically similar as significant changes in surface composition would lead to changes in activation energy. Notably, due to the changes in limiting regime and higher activity and in spite of its lower selectivity, InZrOx-FCC produces MeOH at a higher rate, outperforming InZrOx-BCC at temperatures below 300 °C, finding a maximum difference in terms of absolute MeOH production rate at 275 °C, where InZrOx-FCC reaches a MeOH STY of 0.15 $g_{MeOH}\ h^{-1}\ g_{cat}{}^{-1}$, which is almost double the one produced by InZrOx-BCC at 0.08 $g_{MeOH}\ h^{-1}\ g_{cat}{}^{-1}$.

Table 1. Arrhenius Fit Parameters for the CO_2 Consumption, Direct MeOH Synthesis, and Reverse Water Gas Shift Reactions in InZrOx-FCC and InZrOx-BCC Catalysts

sample	E_a CO_2 consumption (kJ mol^{-1})	E_a MeOH (kJ mol^{-1})	E_a RWGS (kJ mol^{-1})	$\ln(A')$ RWGS
InZrOx-FCC	97 ± 4	114[a]	117 ± 3	21.5 ± 0.5
InZrOx-BCC	129 ± 10	114 ± 3	116 ± 4	19.2 ± 0.9

[a] Calculated with the two data points at 240−250 °C (513−523 K) in the reaction-limited region and only to be taken as a comparison to the activation energy of InZrOx-BCC.

As discussed in the previous section, the CFD simulations showed that the BCC structure leads naturally to a broader residence time distribution and to a shorter average residence time when compared to an FCC structure.[41] This could also explain the higher selectivity of InZrOx-BCC toward MeOH, as the quicker reaction is favored with shorter residence times.[59] Additionally, the weight fraction of elemental indium (In) was measured to be ca. 13.2% in both catalysts (Table S1). A complete characterization of the fabricated catalysts can be found in later sections.

3.3. Composition and Microstructure of Fresh Catalysts.

Following the catalytic performance results, a detailed characterization was carried out on the catalysts to evaluate their elemental and phase composition and porosity, both before and after the catalytic tests.

Figure 5 shows the ex situ synchrotron X-ray diffractograms of InZrOx-E-F. The specimen consists of monoclinic zirconia (m-ZrO_2, PDF 00-036-0420) and cubic indium oxide (c-In_2O_3, PDF 04-010-3287). One minor reflection at 6.36° can be attributed to sodium bentonite. Rietveld refinement results show 7.3 nm c-In_2O_3 crystallites (Table 2) and a 13.2% c-In_2O_3 weight fraction (Table S1).The Rietveld refinement results and ICP-OEM do not fully coincide in the weight fractions of the phases present. To address this issue, two powder mixtures from ZrO_2, In_2O_3, and Na-bentonite were physically made using an agate mortar to serve as references. The powder mixture prepared from 90 wt % ZrO_2, 10 wt % In_2O_3, and 10 wt % Na-bentonite is denoted as Na-Bent-10, while the one prepared from 80 wt % ZrO_2, 10 wt % In_2O_3, and 20 wt % Na-bentonite is named as Na-Bent-20. The

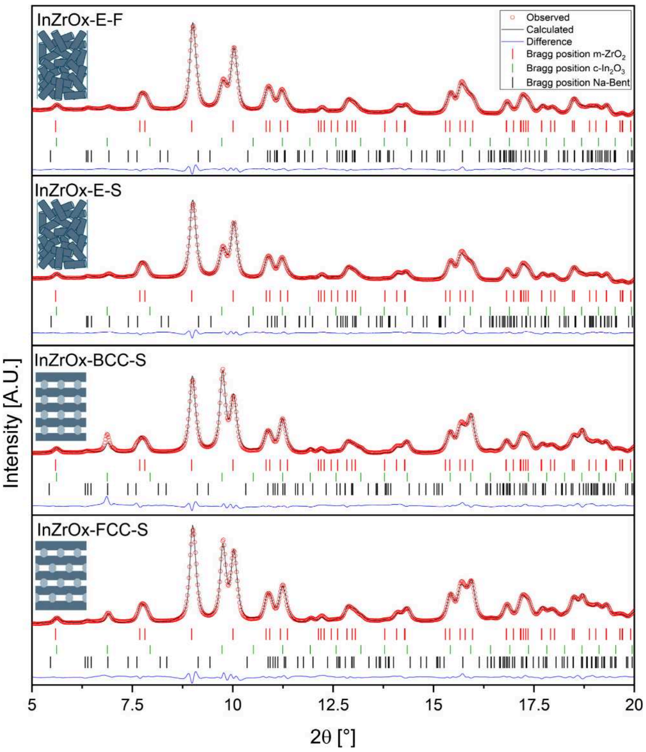

Figure 5. Rietveld refinement analysis of XRD data collected at room temperature (black) of InZrOx-E-F, InZrOx-E-S, InZrOx-BCC-S, and InZrOx-FCC-S, showing the observed (open red circles) and calculated (black line) intensity, difference (blue), and Bragg position of the analyzed phases' calculated reflections (m-ZrO_2, red bars; c-In_2O_3, green bars; and Na-Bent, black bars).

crystalline phase composition of these two reference powders was determined by Rietveld refinement of the XRD data, and the results are shown in Table S2. As can be clearly seen, the weight fractions of sodium bentonite determined from Rietveld refinement are found to be 3.2% and 6.2% in Na-Bent-10 and Na-Bent-20 powder, respectively, indicating that only 31% of crystalline sodium bentonite can be detected by XRD. This can be due to the low crystallinity of the sodium bentonite binder used in this work. This also produces errors in calculating the weight fraction of the remaining phases. Assuming a similar issue arising in InZrOx-E-F (23.2 Na-Bent wt % by ICP-OEM and 5.8 wt % by Rietveld refinement), this discrepancy can be explained. Similar issues arise with the c-In_2O_3 and m-ZrO_2 content, which stem from the underestimation of the amount of Na-Bent. Other laboratory XRD Rietveld refinement results can be seen in Figure S8, where InZrOx-BCC-F and InZrOx-FCC-F show similar reflections, confirming similar phase compositions among all of the tested catalysts.

Newly synthesized fresh catalysts were measured by μXRF and SEM-EDX in order to determine elemental distribution in the whole monolith cross-section and elemental distribution in a strut cross-section, respectively, with the purpose of showing compositional distribution similarity after the fabrication process. Phase distribution was measured through Raman mapping.

Both zirconium (Figure 6a and Figure 6m) and indium (Figure 6b and Figure 6n) appear somewhat homogeneously dispersed in the fresh monoliths. This distribution is similar in both catalyst geometries, showing that the indium coverage is similar across the catalyst and the two samples. Furthermore, the conservation of the BCC and FCC structures can also be seen in these figures.

SEM-EDX measurements on BCC (Figure 6e and Figure 6f) and FCC catalysts (Figure 6q and Figure 6r), were taken to further examine the indium distribution on the catalysts' surface after the synthesis process. As shown, both catalysts have a uniform indium concentration distribution with some more concentrated indium clusters (as c-In_2O_3) both on the surface and along the cross-section. Further single-element maps for all samples can be found in Figure S10.

Complementing the elemental distribution maps, Raman spectroscopy was used to further confirm the distribution of the phases present in the cross-section of the catalysts. Measured reference spectra for c-In_2O_3, m-ZrO_2, $In(OH)_3$, and sodium bentonite are provided in Figure S11 and are in line with literature references.[60−62] A comparison of the obtained baseline-corrected Raman spectra for the catalysts can be found in Figure S12, where they show the same spectral features. The normalized intensity of the main band at 307 cm^{-1} was used as an indicator for c-In_2O_3 concentration and mapped across the catalysts' cross-sections (Figure 6j and Figure 6v). In line with both the μXRF and SEM-EDX maps, the Raman maps show a uniform indium distribution in the fresh samples.

The textural properties of the monoliths were also measured in different stages of the process through nitrogen sorption measurements. The results can be seen in Figure S13 and Figure S14, showing type IV(a) isotherms typical for mesoporous materials. Their classification is not exact as the samples are a mixture of two materials. Calcined sodium bentonite shows an H3 type loop, typical of plate-like

Table 2. Summary of Catalyst Characterization Results for InZrOx-E-F, -E-S, -FCC-F, -FCC-S, -BCC-F, and -BCC-S

	InZrOx-E		InZrOx-FCC		InZrOx-BCC	
	-F	-S	-F	-S	-F	-S
c-In_2O_3 (wt %)[a]	12.0	-	-	15.8	-	16.1
m-ZrO_2 (wt %)[a]	64.8	-	-	62.8	-	62.8[g]
d c-In_2O_3 (nm)[b]	7.25 (±0.011)	8.79 (±0.012)	9.53 (±0.003)	13.65 (±0.015)	10.31 (±0.007)	13.69 (±0.017)
d m-ZrO_2 (nm)[b]	10.74 (±0.008)	11.18 (±0.004)	11.71 (±0.013)	12.06 (±0.009)	11.93 (±0.003)	12.20 (±0.014)
SSA_{BET} (m^2g^{-1})[c]	40	-	37	25	35	32
CO_2 max conversion rate (mol g_{cat}^{-1} h^{-1})[d]	0.0118		0.0246		0.0109	
pressure drop (Pa·m^{-1})	27.6[e]		3.3[f]		2.2[f]	

[a] Measured by ICP-OEM. [b] Crystallite size, determined by Rietveld refinement, with its standard deviation in parentheses. [c] Specific surface area calculated by the BET method. [d] Maximum CO_2 conversion rate achieved in the experiments. [e] Calculated by the Ergün equation. [f] Calculated from CFD results. [g] Assumed to be equal to InZrOx-FCC-S.

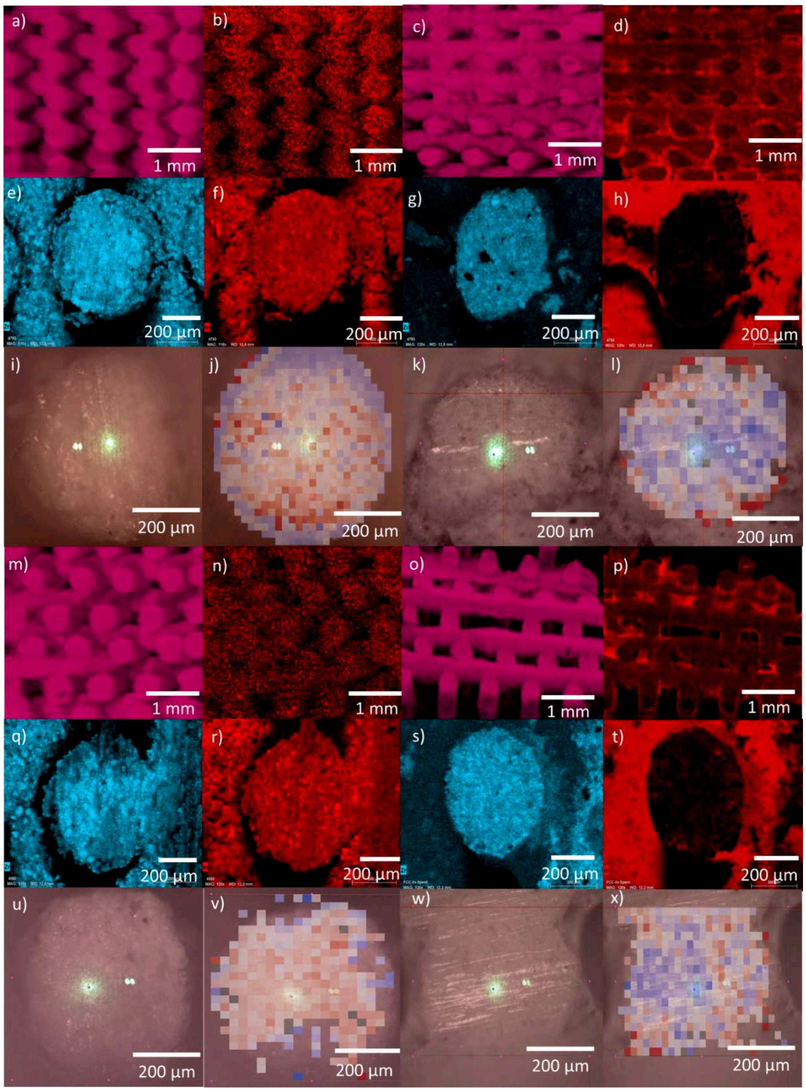

Figure 6. μXRF mapping of Zr (a, c, m, and o) and In (b, d, n, and p) of InZrOx-BCC-F, InZrOx-BCC-S, InZrOx-FCC-F, and InZrOx-FCC-S, respectively. SEM-EDX mapping of Zr (e, g, q, and s) and In (f, h, r, and t) cross-sections of single struts of InZrOx-BCC-F, InZrOx-BCC-S, InZrOx-FCC-F, and InZrOx-FCC-S, respectively. Optical images of Raman-mapped strut cross-sections of InZrOx-BCC-F (i and j), InZrOx-BCC-S (k and l), InZrOx-FCC-F (u and v), and InZrOx-FCC-S (w and x). Raman maps are colored according to the intensity of the 307 cm^{-1} band normalized to the intensity of the 480 cm^{-1} band; each square corresponds to a 20 × 20 μm^2 area. Noncolored sections were excluded from the analysis due to the loss of focus or scattering effects.

particles,[63] whereas the calcined zirconia exhibits a hysteresis loop similar to H1, consistent with the one resulting from the samples, as they are mostly zirconia by weight. These isotherms can be seen in Figure S15. In terms of specific surface area, the supports show very similar results, with ca. 45 $m^2\ g^{-1}$ for the calcined supports before In_2O_3 loading. The S_{BET} slightly drops to ca. 36 $m^2\ g^{-1}$ on the metal-oxide-loaded samples (InZrOx-BCC-F and InZrOx-FCC-F). The reduction in surface area is expected as a consequence of some of the generated indium oxide being accumulated on the inside surfaces of the pores. The structures remain mesoporous, and no significant microporosity can be appreciated.

In summary, the fabrication process generates catalysts that have similar phase and elemental composition as well as similar porous structures and allows us to reasonably exclude the possibility of any of these factors being the source of the different catalytic behavior observed.

3.4. Composition and Microstructure of Spent Catalysts. When InZrOx-E-F and InZrOx-E-S are compared, no changes in the phase composition are observed after the catalytic experiments (Figure 5). Rietveld refinement results, however, point toward some sintering of the indium oxide, with crystallite size increasing from 7.3 to 8.9 nm in InZrOx-E-F and InZrOx-E-S, respectively, which are also slightly larger than the crystallite size in InZrOx-E (Table 2). InZrOx-FCC-S and InZrOx-BCC-S also show the same main phases, with a higher weight fraction of c-In_2O_3 (when compared to InZrOx-E-F and -S), as expected from the ICP-OEM analyses (Table 2). Rietveld refinement results (Table S2) reveal slightly different weight ratios of ZrO_2 and In_2O_3 in all catalysts in comparison to the values determined by the ICP-OEM analysis, which can be explained by the low crystallinity of the sodium bentonite phase that can not be totally detected by XRD, as discussed above.

The zirconium distribution remains unchanged and uniform in both catalysts (Figure 6c and Figure 6o) whereas the indium distribution (Figure 6d and Figure 6p) is significantly altered, with the indium migrating toward the edges of the struts' cross-sections in both catalysts. This effect is seemingly a bit more pronounced in certain areas of the catalysts (especially notable in the lower half of InZrOx-BCC-S in Figure 6d), which may indicate that certain areas of the catalyst are more susceptible to degradation due to being exposed to different environments (as the catalyst is an extended structure and the conditions are not uniform in its volume), and might be connected to the activity difference that the two different structures show. The total c-In_2O_3 contents of InZrOx-FCC-S and InZrOx-BCC-S were obtained through ICP-OEM, yielding 15.8 ± 0.1 and 16.1 ± 0.4 wt %, respectively. The Raman mappings for InZrOx-BCC-S (Figure 6l) and InZrOx-FCC-S (Figure 6x) once again coincide with the μXRF and SEM-EDX maps, showing a depleted center and higher c-In_2O_3 content near the cross-section edges.

The samples also show a reduction in their surface area (Figures S13, S14, and S15), InZrOx-BCC-S from 35 to 32 m^2 g^{-1} and InZrOx-FCC-S from 37 to 25 m^2 g^{-1} (Table 2), possibly due to the sintering of the indium oxide under reaction conditions resulting in narrowing or blocking pores, as described in the previous section. The reduction of indium oxide to indium under reaction conditions with subsequent indium migration toward the surface, oxidation, and sintering has been previously reported,[58] and while the m-ZrO_2 support suppresses it,[64] it is possible that some indium oxide clusters that were not directly impregnated on zirconia contribute to this behavior or that the stronger reducing environment counteracts the stabilization effect of zirconia. To clarify this, in situ XAS measurements of InZrOx-P were carried out (Figure S16). It can be clearly seen that under synchrotron conditions, the InZrOx-P sample starts having spectral features in the postedge region very similar to those of the c-In_2O_3 reference and loses them after prolonged exposure to reaction conditions. Additionally, the edge position shifts to lower energies, indicating some degree of reduction, along with the relative absorption of the edge going down (from 1.4 to 1.2), resembling the behavior of the In^0 foil reference, indicating the reduction of the In_2O_3 catalyst to metallic indium In^0. This reduction has been reported previously for the In_2O_3 catalyst at low conversion conditions,[65] which is expected in the in situ XAS experiment due to the higher WHSV (~300,000 mLs_{Feed} h^{-1} $g_{cat}{}^{-1}$) if compared to that in the reactor used catalytic experiments (50,000 mLs_{Feed} h^{-1} $g_{cat}{}^{-1}$). This behavior is also in line with the results of the literature that were previously discussed.[58] Additionally, InZrOx-FCC-S could be more deteriorated as a consequence of its longer time on stream compared to InZrOx-BCC-S. The higher surface area loss for InZrOx-FCC-S could also be related to the higher concentration of CO produced by the catalyst (Figure 3), which contributes to a more reducing environment, in addition to the higher utilization of the surface (see CFD simulations in Figure 2) when compared to InZrOx-BCC-S, which as mentioned previously seems to have a higher concentration of indium on the surface mainly on the lower half of the catalyst (Figure 6d). Finally, the overall higher activity of InZrOx-FCC could generate higher temperatures on the catalyst surface, which, in turn, promotes catalyst degradation.

4. CONCLUSIONS

In this work, two monoclinic zirconia monoliths with different geometries (straight channeled, BCC, and zig-zag channeled, FCC) were additively manufactured utilizing direct ink writing and postfunctionalized with cubic indium oxide. The effects of the used geometries on gas flow behavior and catalytic performance toward the direct MeOH synthesis were studied.

The obtained results are in line with activity changes measured for other additively manufactured catalytic systems and exhibit degradation pathways at the micrometer scale, consistent with indium reduction, as reported in previous studies.

The CFD simulations show that the flows developed at steady state in the structures differ significantly in terms of velocity distribution and pressure drop, leading to overall thinner boundary layers and a significant reduction of dead zones in the FCC structure, maximizing the accessible surface area.

Catalyst performance studies showed a similar activation energy in both structures toward RWGS (116 kJ mol^{-1}) and direct methanol synthesis (114 kJ mol^{-1}) when evaluated in the kinetic regime, but with a different pre-exponential factor, indicating a higher number of accessible active sites on the InZrOx-FCC structure. The FCC structure showed higher conversion rates and methanol production rates at high WHSV and lower temperatures, while the BCC structure showed better selectivity under those conditions. A comparison with a reference catalyst without a binder shows the negligible contribution of the binder in terms of chemical activity, although physical blocking of sites could take place.

Insight was provided on the effects of exposure to operating conditions. Evidence was found that under these reaction conditions, indium sinters and migrates toward the surface.

The manufactured catalysts could be further tuned by optimizing indium loading, fiber diameter, and channel distance as well as finding some specific binder that might contribute positively to the reaction rates, which could be the object of further work.

■ ASSOCIATED CONTENT

Supporting Information

The Supporting Information is available free of charge at https://pubs.acs.org/doi/10.1021/acs.iecr.4c03439.

Supporting graphs and information (PDF)

Zip file containing the thermodynamic data input file for the iPython notebook (ZIP)

Zip file containing the iPython notebook with the CANTERA code for the recreation of the data used for equilibrium simulations in this work (ZIP)

■ AUTHOR INFORMATION

Corresponding Authors

Emiliano S. Dal Molin − *Technische Universität Berlin, Faculty III Process Sciences, Institute of Material Science and Technology, Chair of Advanced Ceramic Materials, Berlin 10623, Germany*; Email: Emiliano.dalmolin@ceramics.tu-berlin.de

Maged F. Bekheet − *Technische Universität Berlin, Faculty III Process Sciences, Institute of Material Science and Technology, Chair of Advanced Ceramic Materials, Berlin 10623, Germany*; orcid.org/0000-0003-1778-0288; Email: Maged.Bekheet@ceramics.tu-berlin.de

Authors

Mudassar Javed − *Technische Universität Berlin, Process Dynamics and Operations Group, Berlin 10623, Germany*

Georg Brösigke − *Technische Universität Berlin, Process Dynamics and Operations Group, Berlin 10623, Germany;* orcid.org/0000-0003-1104-4087

Maik Alexander Rudolph − *Technische Universität Berlin, Institut für Chemie* − *Technische Chemie, Berlin 10623, Germany*

Jens-Uwe Repke − *Technische Universität Berlin, Process Dynamics and Operations Group, Berlin 10623, Germany*

Reinhard Schomäcker − *Technische Universität Berlin, Institut für Chemie* − *Technische Chemie, Berlin 10623, Germany;* orcid.org/0000-0003-3106-3904

Ulla Simon − *Technische Universität Berlin, Faculty III Process Sciences, Institute of Material Science and Technology, Chair of Advanced Ceramic Materials, Berlin 10623, Germany*

Aleksander Gurlo − *Technische Universität Berlin, Faculty III Process Sciences, Institute of Material Science and Technology, Chair of Advanced Ceramic Materials, Berlin 10623, Germany;* orcid.org/0000-0001-7047-666X

Complete contact information is available at: https://pubs.acs.org/10.1021/acs.iecr.4c03439

Author Contributions

E.S.D.M.: conceptualization, data curation, formal analysis, funding acquisition, investigation, methodology, project administration, software, visualization, and writing−original draft. M.J.: conceptualization, investigation, and writing−review and editing. G.B.: conceptualization, data curation, formal analysis, investigation, methodology, resources, software, and writing−review and editing. M.A.R.: conceptualization, methodology, and writing−review and editing. J.-U.R.: resources and writing−review and editing. R.S.: resources and writing−review and editing. U.S.: conceptualization, methodology, resources, supervision, and writing−review and editing. M.F.B.: conceptualization, formal analysis, funding acquisition, methodology, project administration, resources, supervision, and writing−review and editing. A.G.: conceptualization, funding acquisition, methodology, project administration, resources, supervision, and writing−review and editing.

Notes

The authors declare no competing financial interest.

■ ACKNOWLEDGMENTS

E.S.D.M. was funded by the Einstein Foundation Berlin. This work was partially funded by the Deutsche Forschungsgemeinschaft (DFG German Research Foundation) under Germany's Excellence Strategy EXC2008-390540038 UniSysCat. The authors acknowledge experimental cooperation with Harald Scheel in the Raman group of Christian Thomsen, Festkörperphysik, Fakultät II, at TU Berlin. The authors thank Ferry Schiperski and Cordelia Lange of the MAGMA lab at TU Berlin for their help with XRF measurements and μXRF mapping, as well as Christina Eichenauer from AG Thomas, TU Berlin for nitrogen sorption measurements and Harald Link for ICP-OEM measurements. We acknowledge DESY (Hamburg, Germany), a member of the Helmholtz Association HGF, for the provision of experimental facilities. Parts of this research were carried out at PETRA III and we would like to thank Akhil Tayal and Wolfgang A. Caliebe for assistance in using the P02.1 and P64 beamlines. Beamtime was allocated for the long-term project proposal LTP (II-20210010) and regular proposal (I-20220620). We acknowledge Albert Gili and Benjamin Bischoff for their contribution to the synchrotron measurements. Emiliano Dal Molin thanks Tatiana Mirson for her help with overall graphic design. We acknowledge support by the Open Access Publication Fund of TU Berlin.

■ SYMBOLS USED

A: Arrhenius preexponential factor
A': modified Arrhenius preexponential factor
d_h: hydrodynamic diameter
E_a: activation energy
$\overline{F}$: molar flow
H: particle bed height (or length)
M: molar mass
r: rate of reaction
R_e: Reynolds number
S: selectivity
S: specific surface area
U: gas velocity
V: volume
w: weight
$\overline{w}$: average velocity
X: conversion
x: molar fraction

■ GREEK LETTERS

ε: bed porosity
ρ: density
υ: kinematic viscosity
ζ: friction coefficient

■ SUB- AND SUPERSCRIPTS

0: initial value of the quantity
BET: quantity calculated using the BET model
cat: quantity related to the catalyst
cell: quantity related to the complete simulated cell
eq: quantity at thermodynamic equilibrium
in: value at the reactor inlet
j: quantity value related to substance j
max: maximum thermodynamic achievable rate
out: value at the reactor inlet

■ ABBREVIATIONS

RWGS: reverse water gas shift
STY: space time yield
WHSV: weight hourly space velocity

■ REFERENCES

(1) Goeppert, A.; Czaun, M.; Jones, J.-P.; Surya Prakash, G. K.; Olah, G. A. Recycling of carbon dioxide to methanol and derived products - closing the loop. *Chem. Soc. Rev.* **2014**, *43* (23), 7995−8048.

(2) Asinger, F. *Methanol* — *Chemie- und Energierohstoff*; Springer: Berlin Heidelberg, 1986. DOI: DOI: 10.1007/978-3-642-70763-6.

(3) Reed, T. B.; Lerner, R. M. Methanol: A Versatile Fuel for Immediate Use: Methanol can be made from gas, coal, or wood. It is stored and used in existing equipment. *Science (New York, N.Y.)* **1973**, *182* (4119), 1299−1304.

(4) Olah, G. A. After Oil and Gas: Methanol Economy. *Catal. Lett.* **2004**, *93* (1/2), 1−2.

(5) Zhong, J.; Yang, X.; Wu, Z.; Liang, B.; Huang, Y.; Zhang, T. State of the art and perspectives in heterogeneous catalysis of CO2 hydrogenation to methanol. *Chem. Soc. Rev.* **2020**, *49* (5), 1385−1413.

(6) Fang, Y.; Wang, F.; Chen, Y.; Lv, Q.; Jiang, K.; Yang, H.; Zhao, H.; Wang, P.; Gan, Y.; Wu, L.; Tang, Y.; Gao, X.; Tan, L. Realizing methanol synthesis from CO and water via the synergistic effect of Cu0/Cu+ over Cu/ZrO2 catalyst. *Journal of Energy Chemistry* **2024**, *93*, 126−134.

(7) Zhao, H.; Yu, R.; Ma, S.; Xu, K.; Chen, Y.; Jiang, K.; Fang, Y.; Zhu, C.; Liu, X.; Tang, Y.; Wu, L.; Wu, Y.; Jiang, Q.; He, P.; Liu, Z.; Tan, L. The role of Cu1−O3 species in single-atom Cu/ZrO2 catalyst for CO2 hydrogenation. *Nat. Catal* **2022**, *5* (9), 818−831.

(8) Frei, M. S.; Capdevila-Cortada, M.; García-Muelas, R.; Mondelli, C.; López, N.; Stewart, J. A.; Curulla Ferré, D.; Pérez-Ramírez, J. Mechanism and microkinetics of methanol synthesis via CO2 hydrogenation on indium oxide. *J. Catal.* **2018**, *361*, 313−321.

(9) Frei, M. S.; Mondelli, C.; Cesarini, A.; Krumeich, F.; Hauert, R.; Stewart, J. A.; Curulla Ferré, D.; Pérez-Ramírez, J. Role of Zirconia in Indium Oxide-Catalyzed CO 2 Hydrogenation to Methanol. *ACS Catal.* **2020**, *10* (2), 1133−1145.

(10) Yu, Y.; Lin, G.; Song, W.; Wang, J.; Chen, H.; Fu, J.; Lou, Y. Strong Cu/ZnO Interfacial Interaction Induced by ZrO 2 Promoter Suppressing the Ethanol Formation in Industrial Methanol Synthesis. *Ind. Eng. Chem. Res.* **2024**, *63* (28), 12459−12467.

(11) Martin, O.; Martín, A. J.; Mondelli, C.; Mitchell, S.; Segawa, T. F.; Hauert, R.; Drouilly, C.; Curulla-Ferré, D.; Pérez-Ramírez, J. Indium Oxide as a Superior Catalyst for Methanol Synthesis by CO2 Hydrogenation. *Angewandte Chemie (International ed. in English)* **2016**, *55* (21), 6261−6265.

(12) Chen, T.; Cao, C.; Chen, T.; Ding, X.; Huang, H.; Shen, L.; Cao, X.; Zhu, M.; Xu, J.; Gao, J.; Han, Y.-F. Unraveling Highly Tunable Selectivity in CO 2 Hydrogenation over Bimetallic In-Zr Oxide Catalysts. *ACS Catal.* **2019**, *9* (9), 8785−8797.

(13) Sun, K.; Fan, Z.; Ye, J.; Yan, J.; Ge, Q.; Li, Y.; He, W.; Yang, W.; Liu, C. Hydrogenation of CO2 to methanol over In2O3 catalyst. *Journal of CO2 Utilization* **2015**, *12*, 1−6.

(14) Wang, J.; Zhang, G.; Zhu, J.; Zhang, X.; Ding, F.; Zhang, A.; Guo, X.; Song, C. CO 2 Hydrogenation to Methanol over In 2 O 3 -Based Catalysts: From Mechanism to Catalyst Development. *ACS Catal.* **2021**, *11* (3), 1406−1423.

(15) Ye, R.-P.; Ding, J.; Gong, W.; Argyle, M. D.; Zhong, Q.; Wang, Y.; Russell, C. K.; Xu, Z.; Russell, A. G.; Li, Q.; Fan, M.; Yao, Y.-G. CO2 hydrogenation to high-value products via heterogeneous catalysis. *Nat. Commun.* **2019**, *10* (1), 5698.

(16) Shi, Y.; Gu, Q.; Zhao, Y.; Ren, Y.; Yang, B.; Xu, J.; Zhang, Y.; Pan, C.; Zhu, Y.; Lou, Y. Local In-O-Pd Lewis acid-base pair boosting CO2 selective hydrogenation to methanol. *Chemical Engineering Journal* **2024**, *485*, No. 150093.

(17) Bogdan, E.; Michorczyk, P. 3D Printing in Heterogeneous Catalysis-The State of the Art. *Materials (Basel, Switzerland)* **2020**, *13* (20), 4534.

(18) Hartings, M. R.; Ahmed, Z. Chemistry from 3D printed objects. *Nat. Rev. Chem.* **2019**, *3* (5), 305−314.

(19) Hurt, C.; Brandt, M.; Priya, S. S.; Bhatelia, T.; Patel, J.; Selvakannan, P.; Bhargava, S. Combining additive manufacturing and catalysis: a review. *Catal. Sci. Technol.* **2017**, *7* (16), 3421−3439.

(20) Peng, E.; Zhang, D.; Ding, J. Ceramic Robocasting: Recent Achievements, Potential, and Future Developments. *Advanced materials (Deerfield Beach, Fla.)* **2018**, *30* (47), No. e1802404.

(21) Smay, J. E.; Gratson, G. M.; Shepherd, R. F.; Cesarano, J.; Lewis, J. A. Directed Colloidal Assembly of 3D Periodic Structures. *Adv. Mater.* **2002**, *14* (18), 1279−1283.

(22) Smay, J. E.; Cesarano, J.; Lewis, J. A. Colloidal Inks for Directed Assembly of 3-D Periodic Structures. *Langmuir* **2002**, *18* (14), 5429−5437.

(23) Laguna, O. H.; Lietor, P. F.; Godino, F. I.; Corpas-Iglesias, F. A. A review on additive manufacturing and materials for catalytic applications: Milestones, key concepts, advances and perspectives. *Materials & Design* **2021**, *208*, No. 109927.

(24) Parra-Cabrera, C.; Achille, C.; Kuhn, S.; Ameloot, R. 3D printing in chemical engineering and catalytic technology: structured catalysts, mixers and reactors. *Chem. Soc. Rev.* **2018**, *47* (1), 209−230.

(25) Ferrizz, R. M.; Stuecker, J. N.; Cesarano, J.; Miller, J. E. Monolithic Supports with Unique Geometries and Enhanced Mass Transfer. *Ind. Eng. Chem. Res.* **2005**, *44* (2), 302−308.

(26) Stuecker, J. N.; Miller, J. E.; Ferrizz, R. E.; Mudd, J. E.; Cesarano, J. Advanced Support Structures for Enhanced Catalytic Activity. *Ind. Eng. Chem. Res.* **2004**, *43* (1), 51−55.

(27) Middelkoop, V.; Vamvakeros, A.; de Wit, D.; Jacques, S. D.M.; Danaci, S.; Jacquot, C.; de Vos, Y.; Matras, D.; Price, S. W.T.; Beale, A. M. 3D printed Ni/Al2O3 based catalysts for CO2 methanation - a comparative and operando XRD-CT study. *Journal of CO2 Utilization* **2019**, *33*, 478−487.

(28) Zhou, X.; Liu, C. Three-dimensional Printing for Catalytic Applications: Current Status and Perspectives. *Adv. Funct. Mater.* **2017**, *27* (30), No. 1701134.

(29) Rosseau, L. R.; Middelkoop, V.; Willemsen, H. A.; Roghair, I.; van Sint Annaland, M. Review on Additive Manufacturing of Catalysts and Sorbents and the Potential for Process Intensification. *Front. Chem. Eng.* **2022**, *4*, n/a.

(30) Danaci, S.; Protasova, L.; Lefevere, J.; Bedel, L.; Guilet, R.; Marty, P. Efficient CO 2 methanation over Ni/Al 2 O 3 coated structured catalysts. *Catal. Today* **2016**, *273*, 234−243.

(31) Díaz-Marta, A. S.; Yañez, S.; Lasorsa, E.; Pacheco, P.; Tubío, C. R.; Rivas, J.; Piñeiro, Y.; Gómez, M. A. G.; Amorín, M.; Guitián, F.; Coelho, A. Integrating Reactors and Catalysts through Three-Dimensional Printing: Efficiency and Reusability of an Impregnated Palladium on Silica Monolith in Sonogashira and Suzuki Reactions. *ChemCatChem.* **2020**, *12* (6), 1762−1771.

(32) Díaz-Marta, A. S.; Tubío, C. R.; Carbajales, C.; Fernández, C.; Escalante, L.; Sotelo, E.; Guitián, F.; Barrio, V. L.; Gil, A.; Coelho, A. Three-Dimensional Printing in Catalysis: Combining 3D Heterogeneous Copper and Palladium Catalysts for Multicatalytic Multicomponent Reactions. *ACS Catal.* **2018**, *8* (1), 392−404.

(33) Alimi, O. A.; Akinnawo, C. A.; Meijboom, R. Monolith catalyst design via 3D printing: a reusable support for modern palladium-catalyzed cross-coupling reactions. *New J. Chem.* **2020**, *44* (43), 18867−18878.

(34) Magzoub, F.; Li, X.; Lawson, S.; Rezaei, F.; Rownaghi, A. A. 3D-printed HZSM-5 and 3D-HZM5@SAPO-34 structured monoliths with controlled acidity and porosity for conversion of methanol to dimethyl either. *Fuel* **2020**, *280*, No. 118628.

(35) Lefevere, J.; Mullens, S.; Meynen, V. The impact of formulation and 3D-printing on the catalytic properties of ZSM-5 zeolite. *Chemical Engineering Journal* **2018**, *349*, 260−268.

(36) Ben-Arfa, B. A. E.; Abanades, S.; Salvado, I. M. M.; Ferreira, J. M. F.; Pullar, R. C. Robocasting of 3D printed and sintered ceria scaffold structures with hierarchical porosity for solar thermochemical fuel production from the splitting of CO2. *Nanoscale* **2022**, *14* (13), 4994−5001.

(37) Karsten, T.; Middelkoop, V.; Matras, D.; Vamvakeros, A.; Poulston, S.; Grosjean, N.; Rollins, B.; Gallucci, F.; Godini, H. R.; Jacques, S. D. M.; Beale, A. M.; Repke, J.-U. Multi-Scale Studies of 3D Printed Mn−Na−W/SiO2 Catalyst for Oxidative Coupling of Methane. *Catalysts* **2021**, *11* (3), 290.

(38) Michorczyk, P.; Hędrzak, E.; Węgrzyniak, A. Preparation of monolithic catalysts using 3D printed templates for oxidative coupling of methane. *J. Mater. Chem. A* **2016**, *4* (48), 18753−18756.

(39) Lefevere, J.; Gysen, M.; Mullens, S.; Meynen, V.; van Noyen, J. The benefit of design of support architectures for zeolite coated structured catalysts for methanol-to-olefin conversion. *Catal. Today* **2013**, *216*, 18−23.

(40) Lefevere, J.; Protasova, L.; Mullens, S.; Meynen, V. 3D-printing of hierarchical porous ZSM-5: The importance of the binder system. *Materials & Design* **2017**, *134*, 331−341.

(41) Rosseau, L. R.; Jansen, J. T.; Roghair, I.; van Sint Annaland, M. Favorable trade-off between heat transfer and pressure drop in 3D printed baffled logpile catalyst structures. *Chem. Eng. Res. Des.* **2023**, *196*, 214−234.

(42) Kopperschmidt, P. Tetragonal photonic woodpile structures. *Applied Physics B: Lasers and Optics* **2003**, *76* (7), 729−734.

(43) *Proccedings of 11th International Conference Biomdlore 2016*; Griškevičius, J., Ed.; VGTU Technika, 2016.

(44) Bekheet, M. F.; Schwarz, M. R.; Müller, M. M.; Lauterbach, S.; Kleebe, H.-J.; Riedel, R.; Gurlo, A. Phase segregation in Mn-doped In2O3: in situ high-pressure high-temperature synchrotron studies in multi-anvil assemblies. *RSC Adv.* **2013**, *3* (16), 5357.

(45) Dal Molin, E. S.; Henning, L. M.; Müller, J. T.; Smales, G. J.; Pauw, B. R.; Bekheet, M. F.; Gurlo, A.; Simon, U. Robocasting of ordered mesoporous silica-based monoliths: Rheological, textural, and mechanical characterization. *Nano Select* **2023**, *4* (11−12), 615.

(46) Pang, S.; Wu, D.; Gurlo, A.; Kurreck, J.; Hanaor, D. A. H. Additive manufacturing and performance of bioceramic scaffolds with different hollow strut geometries. *Biofabrication* **2023**, *15* (2), 025011.

(47) Rodriguez-Carvajal, J. FULLPROF: A Program for Rietveld Refinement and Pattern Matching Analysis. In *Abstracts of the Satellite Meeting on Powder Diffraction of the XV Congress of the IUCr*, Toulouse, France, 1990; pp 127.

(48) Finger, L. W.; Cox, D. E.; Jephcoat, A. P. A correction for powder diffraction peak asymmetry due to axial divergence. *J. Appl. Crystallogr.* **1994**, *27* (6), 892−900.

(49) Eilers, P. H. C. A perfect smoother. *Analytical chemistry* **2003**, *75* (14), 3631−3636.

(50) Afseth, N. K.; Kohler, A. Extended multiplicative signal correction in vibrational spectroscopy, a tutorial. *Chemometrics and Intelligent Laboratory Systems* **2012**, *117*, 92−99.

(51) Toplak, M.; Birarda, G.; Read, S.; Sandt, C.; Rosendahl, S. M.; Vaccari, L.; Demšar, J.; Borondics, F. Infrared Orange: Connecting Hyperspectral Data with Machine Learning. *Synchrotron Radiation News* **2017**, *30* (4), 40−45.

(52) Toplak, M.; Read, S. T.; Sandt, C.; Borondics, F. Quasar: Easy Machine Learning for Biospectroscopy. *Cells* **2021**, *10* (9), 2300.

(53) Caliebe, W. A.; Murzin, V.; Kalinko, A.; Görlitz, M. High-flux XAFS-beamline P64 at PETRA III. *AIP Conf. Proc.* **2019**, *2054* (1), 060031.

(54) Bischoff, B.; Bekheet, M. F.; Dal Molin, E.; Praetz, S.; Kanngießer, B.; Schomäcker, R.; Etter, M.; Jeppesen, H. S.; Tayal, A.; Gurlo, A.; Gili, A. In situ/operando plug-flow fixed-bed cell for synchrotron PXRD and XAFS investigations at high temperature, pressure, controlled gas atmosphere and ultra-fast heating. *J. Synchrotron Radiat.* **2023**, *31* (1), 77−84.

(55) Goodwin, D. G.; Moffat, H. K.; Schoegl, I.; Speth, R. L.; Weber, B. W. *Cantera: An Object-oriented Software Toolkit for Chemical Kinetics, Thermodynamics, and Transport Processes*; Zenodo, 2022.

(56) Khan, W. A.; Culham, J. R.; Yovanovich, M. M. Convection heat transfer from tube banks in crossflow: Analytical approach. *Int. J. Heat Mass Transfer* **2006**, *49* (25−26), 4831−4838.

(57) Rosseau, L. R.; Schinkel, M. A.; Roghair, I.; van Sint Annaland, M. Experimental Quantification of Gas Dispersion in 3D-Printed Logpile Structures Using a Noninvasive Infrared Transmission Technique. *ACS Eng. Au* **2022**, *2* (3), 236−247.

(58) Tsoukalou, A.; Serykh, A. I.; Willinger, E.; Kierzkowska, A.; Abdala, P. M.; Fedorov, A.; Müller, C. R. Hydrogen dissociation sites on indium-based ZrO2-supported catalysts for hydrogenation of CO2 to methanol. *Catal. Today* **2022**, *387*, 38−46.

(59) Fogler, H. S. *Essentials of Chemical Reaction Engineering*, 2nd ed.; Prentice Hall International Series in the Physical and Chemical Engineering Sciences; Prentice Hall, 2018.

(60) Gurlo, A.; Dzivenko, D.; Andrade, M.; Riedel, R.; Lauterbach, S.; Kleebe, H.-J. Pressure-induced decomposition of indium hydroxide. *J. Am. Chem. Soc.* **2010**, *132* (36), 12674−12678.

(61) Yang, J.; Frost, R. L.; Martens, W. N. Thermogravimetric analysis and hot-stage Raman spectroscopy of cubic indium hydroxide. *J. Therm Anal Calorim* **2010**, *100* (1), 109−116.

(62) Basahel, S. N.; Ali, T. T.; Mokhtar, M.; Narasimharao, K. Influence of crystal structure of nanosized ZrO2 on photocatalytic degradation of methyl orange. *Nanoscale Res. Lett.* **2015**, *10*, 73.

(63) Thommes, M.; Kaneko, K.; Neimark, A. V.; Olivier, J. P.; Rodriguez-Reinoso, F.; Rouquerol, J.; Sing, K. S. Physisorption of gases, with special reference to the evaluation of surface area and pore size distribution (IUPAC Technical Report). *Pure Appl. Chem.* **2015**, *87* (9−10), 1051−1069.

(64) Zhang, X.; Kirilin, A. V.; Rozeveld, S.; Kang, J. H.; Pollefeyt, G.; Yancey, D. F.; Chojecki, A.; Vanchura, B.; Blum, M. Support Effect and Surface Reconstruction in In 2 O 3/m- ZrO 2 Catalyzed CO 2 Hydrogenation. *ACS Catal.* **2022**, *12* (7), 3868−3880.

(65) Kampe, P.; Wesner, A.; Schühle, P.; Hess, F.; Albert, J. Effect of Conversion, Temperature and Feed Ratio on In2 O3 /In(OH)3 Phase Transitions in Methanol Synthesis Catalysts: A Combined Experimental and Computational Study. *ChemPlusChem.* **2023**, *88* (9), No. e202300425.